Wear 342-343 (2015) 270–278

Contents lists available at ScienceDirect

Wear

journal homepage: www.elsevier.com/locate/wear

Nanotribological, nanomechanical and interfacial characterization of atomic layer deposited TiO_2 on a silicon substrate ☆

Jussi Lyytinen [a,*], Xuwen Liu [a], Oili M.E. Ylivaara [c], Sakari Sintonen [b], Ajai Iyer [a], Saima Ali [a], Jaakko Julin [d], Harri Lipsanen [b], Timo Sajavaara [d], Riikka L. Puurunen [c], Jari Koskinen [a]

[a] Aalto University School of Chemical Technology, Department of Materials Science and Engineering, P. O. Box 16200, FI-00076 Aalto, Finland
[b] Aalto University School of Electrical Engineering, Department of Micro- and Nanosciences, P. O. Box 13500, FI-00076 Aalto, Finland
[c] VTT Technical Research Centre of Finland, P. O. Box 1000, FI-02044 Espoo, Finland
[d] University of Jyväskylä, Department of Physics, P. O. Box 35, FI-40014 Jyväskylä, Finland

ARTICLE INFO

Article history:
Received 17 July 2015
Received in revised form
1 September 2015
Accepted 3 September 2015
Available online 11 September 2015

Keywords:
Nanotribology
Nanoscratch
Scanning nanowear
Nanomechanical characterization
Interfacial characterization
Atomic layer deposition

ABSTRACT

For every coating it is critical that the coatings are sufficiently durable to withstand practical applications and that the films adhere well enough to the substrate. In this paper the nanotribological, nanomechanical and interfacial properties of 15–100 nm thick atomic layer deposited (ALD) TiO_2 coatings deposited at 110–300 °C were studied using a novel combination of nanoscratch and scanning nanowear testing. Thin film wear increased linearly with increasing scanning nanowear load. The film deposited at 300 °C was up to 58 ± 11 %-points more wear-resistant compared to the films deposited at lower temperatures due to higher hardness and crystallinity of the film. Amorphous/nanocrystalline composite structure with agglomerated crystallites was observed with TiO_2 deposited at 200 °C and the agglomerates were up to 37 ± 10%-points more wear-resistant than the amorphous/nanocrystalline matrix. All of the tested films had excellent interfacial properties and no delamination was observed with the films outside of the scanned regions. These findings may prove useful in the development of tribological and mechanical characterization methods, and in developing thin film materials with enhanced properties tailored to their function. This will also help in the development and tuning of ALD processes.

1. Introduction

Highly conformal coatings down to the thickness of a fraction of a monolayer can be produced by atomic layer deposition (ALD) even on complex three-dimensional topographies [1–3]. ALD is one of the most rapidly developing fields of thin film technology belonging to the general class of chemical vapor deposition (CVD) techniques [4]. Typical applications for ALD-films include semiconductor devices such as high dielectric constant gate oxides in the MOSFET structure, copper diffusion barriers in backend interconnects, energy applications as well as micro- and nanoelectromechanical systems (MEMS/NEMS) [5,6]. TiO_2 thin films are used in a wide variety of applications: photovoltaic devices such as solar cells [7,8], corrosion resistance [9], self-cleaning [10], water purification [11], anti-fogging [12], superhydrophilicity [13], as well as anti-bacterial [14], -fungal [15] and -algal [16] applications.

Thin film characteristics, performance and practical usability are highly dependent on good interfacial properties, such as film-substrate adhesion of the coatings. Delamination or film breakage may occur if the film does not adhere well enough to the substrate, degrading the film performance or rendering them useless. Interfacial characterization of films in the sub 100 nm region can be challenging and there is no universal technique or analysis approach to determine the interfacial toughness. Common methods for testing the interfacial mechanical properties such as adhesion of thin films to their substrate are scratch testing, pull-off testing, indentation testing, blister testing and bend testing. For

*JL was responsible of the research plan for the nanotribological, nanomechanical and interfacial testing, designing and performing the experiments and analyzing the results. JL made all of the SEM characterization and analysis and wrote the manuscript under the supervision of JK. XWL was responsible for the nanoindentation measurements and he also helped with the nanotribological, nanomechanical and interfacial testing. OMEY fabricated the samples and made the residual stress measurements and analysis under the supervision of RLP, who also contributed greatly in the design of the sample matrix. SS and SA made GIXRD and XRR measurements and analysis under supervision of HL. JJ made TOF-ERDA measurements and analysis under supervision of TS. AI helped with the literature review and commented on the manuscript. Authors doing the measurements discussed the results and implications and commented on the manuscript by JL at all stages.

* Corresponding author.
E-mail address: Jussi.Lyytinen@Aalto.fi (J. Lyytinen).

http://dx.doi.org/10.1016/j.wear.2015.09.001
0043-1648/

testing the tribological properties, such as wear resistance, pin-on-disc testing and reciprocating wear testing are often used [17–20].

Micro- and nanorobotics combined with force measurement and characterization can be used to measure the mechanical properties of micro- and nanostructures [21]. Specifically, if the thin films have low adhesion to the substrate, shaft-loaded blister testing can be used to quantitatively define the interfacial properties [22]. On the other hand, if the thin films have excellent adhesion to the substrate, embedded microspheres can be used to quantitatively study the interfacial properties [23,24]. The embedded microsphere approach focuses the loading to the thin film and minimizes the effect of the substrate. Another way to minimize the interaction volume of the loading to the substrate is to use scanning nanowear with a sharp tip with increasing load while observing the wear and fracture of the thin film as well as the interfacial behavior [25]. In this paper, 15–100 nm thick atomic layer deposited TiO_2 thin films are characterized using the scanning nanowear approach. The method is complemented with an initial nanoscratch from the top of the films down to the film-substrate interface to facilitate thin film delamination. ALD films have potential use in various kinds of protective applications where they are subjected to wear, yet their mechanical properties have remained poorly studied. This paper is thus filling an important vacancy in knowledge with a systematic study of the nanotribological, nanomechanical and interfacial properties of ALD TiO_2 thin films. The test method is generic and it can be applied to practically any thin films (within reasonable limits for film thickness and roughness). An example of a practical application for the method would be to study a MEMS component with moving parts undergoing wear.

2. Experimental

2.1. Sample preparation

ALD films were grown on 150 mm p-type (100) single side polished (SSP) silicon wafers with thickness of 675 ± 15 μm in an ISO 4 cleanroom. Silicon wafers were wet cleaned before deposition using RCA cleaning (SC-1, DHF and SC-2) followed by deionized water rinses between the cleaning baths and spin-drying at the end of cleaning cycle to get controlled surface conditions for further processing.

Films were grown in Picosun™ R-150 top-flow ALD reactor, with the $TiCl_4$–H_2O process ($TiCl_4$ precursor from SAFC Hitech, Electronic grade). The process pressure was about 10 hPa with constant 200 sccm nitrogen (purity $>99.999\%$) flow through reactant lines. The following deposition process was used: 0.1 s $TiCl_4$ – 4.0 s purge – 0.1 s H_2O – 4.0 s purge. The deposition temperature and the target/measured thickness can be seen in Table 1 for all of the samples. The number of ALD cycles was varied from about 300 to 2500 depending on the target thickness based on previous optimization. Growth to the backside of the wafer was prevented by protecting the backside with 150 mm SSP wafer, rough side against the backside. Despite the backside protection a visible 1–5 mm edge ring was grown on the backside of the wafers. Film thicknesses were measured after ALD deposition using FilmTek 2000 M spectroscopic reflectometry in a 49-point automated measurement with the accuracy of 0.8% based on repeatability testing of the instrument. The calibration of the reflectometry was done using internal and manufacturer supplied reference samples. The instrument is most reliable with films with the thickness of over 50 nm.

Table 1
Experimental matrix and sample codes of different types of TiO_2 thin films. Thickness measured using reflectometry. (Note that the 300 °C, 100 nm sample C is included in both the temperature and the thickness series).

Sample	Test series	Deposition temperature (°C)	Target thickness (nm)	Measured thickness (nm)	Number of cycles
A	Temperature	110	100	95.7 ± 2.4	1924
B	Temperature	200	100	92.8 ± 3.4	2467
C	Temperature/ Thickness	300	100	101.5 ± 1.0	2124
D	Thickness	300	50	48.3 ± 0.6	1062
E	Thickness	300	15	13.0 ± 0.6	319

2.2. X-ray reflectivity (XRR) and grazing incidence diffraction (GIXRD) measurement for film thickness, density and crystallinity

The thickness (also measured using reflectometry), density and roughness were measured using X-ray reflectivity (XRR) and the crystallinity was measured using grazing incidence X-ray diffractometry (GIXRD). The measurement instrument was a Philips X'Pert Pro diffractometer using Cu Kα radiation (wavelength 1.54 Å) with 40 kV acceleration voltage and 40 mA current. The XRR results are based on simulations and thus the accuracy is case dependent. The measurement setup and conditions were identical to those reported earlier [26].

2.3. Wafer curvature measurement for residual stress

Residual stress was calculated using wafer curvature method, as described earlier [25]. The curvature was measured before and after ALD deposition using a Veeco DEKTAK V200-Si stylus profilometer. Wafers were scanned parallel and perpendicular to the wafer flat using 120 mm scan length. The stress was determined using Veeco's Stress Measurement Analysis software that uses Stoney's equation [27]

$$\sigma_f = -\frac{E_s}{6(1-\upsilon_s)}\frac{t_s^2}{t_f}\left(\frac{1}{R_1}-\frac{1}{R_0}\right), \quad (1)$$

where σ_f is the thin film stress [Pa] (negative for compressive stress), E_s is the elastic modulus of the substrate [Pa], υ_s is Poisson's ratio of the substrate, R_0 and R_1 are the radius of curvature before and after the film growth [m], respectively, and t_s and t_f are the thicknesses of the substrate and the film [m]. $E_s/(1-\upsilon_s)$ is a biaxial modulus having a constant value of 1.805×10^{11} Pa for (100) Si [28]. The error values represent the maximum error calculated through partial differential method as described earlier [15], taking into account the effect of absolute substrate and film thickness as well as the uncertainty in the substrate thickness, film thickness and wafer bow measurement.

2.4. Time-of-flight elastic recoil detection analysis (TOF-ERDA) measurements for film composition and impurity concentration

The film composition and impurities were analyzed using time-of-flight elastic recoil detection analysis (TOF-ERDA). The self-built equipment uses 10.2 MeV ^{35}Cl and 11.9 MeV ^{63}Cu ions from a 1.7 MV Pelletron accelerator [29]. TOF-ERDA enables quantitative detection and depth profiling of hydrogen and other light elements in addition to the heavy ones.

2.5. Nanoindentation for hardness and elastic modulus

Nanoindentation was carried out using Hysitron TriboIndenter® TI-900 nanomechanical testing system. Indentations

were performed under load-controlled mode using loading, holding at peak-load and unloading segment times of 10, 5 and 5 s, respectively. A North-Star cube-corner diamond tip with a 90° total induced angle and a vendor specified nominal tip radius of under 40 nm was used in the measurements. The tip radius will increase over time as the tip wears out and the tip area function is checked regularly. The purpose of using a sharp tip (compared to a 120° total induced angle Berkovich tip) was to trigger plastic deformation at shallow indents, less than 10% of the film thickness, to measure the film hardness with minimal substrate effects.

The mechanical properties were extracted from a series of load and depth data using the Oliver and Pharr method [30], where the elastic modulus of the film, E_f and the substrate, E_i are related to the contact modulus, E^*, through the following equation

$$\frac{1}{E^*}=\frac{1-\upsilon_i^2}{E_i}+\frac{1-\upsilon_f^2}{E_f}, \tag{2}$$

where ν_i and ν_f are Poisson's ratio for the diamond tip and grown film, respectively. For diamond tip, $E_i=1140$ GPa and $\nu_i=0.07$. Poisson's ratio of $\nu_{TiO2}=0.28$ was used for the TiO_2 films. The hardness of the film is defined as the maximum indentation load divided by the contact area corresponding to the load [31]

$$H=\frac{P_{max}}{A}. \tag{3}$$

The instrument stability and indentation repeatability were monitored by performing a series of 16 indents into a piece of silicon wafer over a period of time with the peak load varying from 5 to 500 μN. The silicon reference sample was taken from the same wafer batch that was used as the substrate for the TiO_2 films. The indenter conditions (tip rounding) were also checked throughout the measurement by indenting on the standard fused quartz to see the need of the tip area function for recalibration but the tip-radius was not measured directly.

2.6. Nanoscratch and scanning nanowear for nanotribological and interfacial properties

Nanotribological measurements were also carried out using Hysitron TriboIndenter® TI-900 nanomechanical testing system. A North-Star cube-corner diamond tip with a 90° total induced angle and a vendor specified nominal tip radius of under 40 nm was used in the measurements. A combination of nanoscratch and scanning nanowear was used to study the nanotribological and interfacial properties of the films. First an initiation point for possible interfacial failure was generated by 8 μm long tilt-corrected displacement controlled nanoscratching from the top of the coating down to the film-substrate interface. Scanning nanowear with 10–40 μN loads, 256 scan lines, 2 Hz frequency and 24 μm/s tip velocity was then used at an area of 12 × 12 μm around the scratches for film wear analysis and to see if interfacial failure would occur from the pre-scratch (each nanowear load was tested on a separate area). Finally the tested region was imaged using the same tip with the inbuilt scanning probe microscopy (SPM) of the nanoindenter at an area of 15 × 15 μm using 1.5 μN imaging load, 1 Hz frequency and 15 μm/s tip velocity. After the nanotribological measurements the samples were imaged using TESCAN MIRA3 FEG scanning electron microscope (SEM) for more detailed characterization.

3. Results

3.1. Film thickness, density and crystallinity

The film thickness, density and roughness were measured using XRR. The crystallinity was measured using GIXRD and the results are listed in Table 2. The incidence angle of the GIXRD was slightly higher than the critical angle of total reflection while the exit angle was scanned over a wide angular range of $2\theta=20$–$100°$. The film thickness measured by XRR is similar to reflectometry within a few nanometers difference caused by film roughness and inherent differences in the measurement techniques.

SEM and SPM showed crystallite agglomerates in sample B (200 °C, 100 nm) that protrude up to 70 nm from the amorphous/nanocrystalline matrix level as seen in Fig. 1. GIXRD measurements showed anatase peaks for all of the samples besides A (110 °C, 100 nm).

3.2. Film composition and impurity concentration

The film composition and impurity concentration were measured from the 100 nm thick films using TOF-ERDA and the results are listed in Table 3. The statistical error for Ti and O compositions is small but systematic error due to stopping forces can take place. For small concentrations, the statistical uncertainty is dominant and can be estimated to be about 20% for hydrogen and 20–40% for carbon. The quantification limit for carbon is about 0.05 at%. Films under 100 nm were not measured and the film composition was expected to be the same as with 100 nm. When measuring thinner films with TOF-ERDA careful analysis is needed as the separation of impurities from the interface and the substrate becomes more difficult increasing the error limits and uncertainty of the measurement results which might lead to higher than true impurity concentrations. At lower temperatures the films had more hydrogen and chlorine impurities compared to the more pure film deposited at 300 °C. All of the films were stoichiometric TiO_2.

3.3. Hardness, elastic modulus and residual stress

The hardness and elastic modulus of the samples were measured by nanoindentation and the results are listed in Table 4. The error limits are the standard deviation of at least 16 repeated indentations. The residual stress was measured using contact profilometry and the results are listed in Table 4. The error values represent the maximum error calculated through partial differential method as described earlier [25], taking into account the effect of absolute substrate and film thickness as well as the uncertainty in the substrate thickness, film thickness and wafer bow measurement.

Table 2
Results of XRR and GIXRD: measured film thicknesses, density, roughness and crystallinity. The anatase crystalline phase was observed in samples grown at 200 °C and above. No other crystalline phase was observed.

Sample (temp, thickness)	Thickness (nm)	Density (g/cm^3)	Roughness (nm)	Crystallinity
A (110 °C, 100 nm)	97.3	3.70	0.5	Amorphous
B (200 °C, 100 nm)	90.5	3.80	0.5	Amorphous/Anatase
C (300 °C, 100 nm)	91.5	3.80	4.3	Anatase
D (300 °C, 50 nm)	45.5	3.80	3.3	Anatase[a]
E (300 °C, 15 nm)	11.9	3.80	1.0	Anatase[a]

[a] For 50 nm film only the (101) and (200) peaks were observed and for the 15 nm film only the (101) peak was observed.

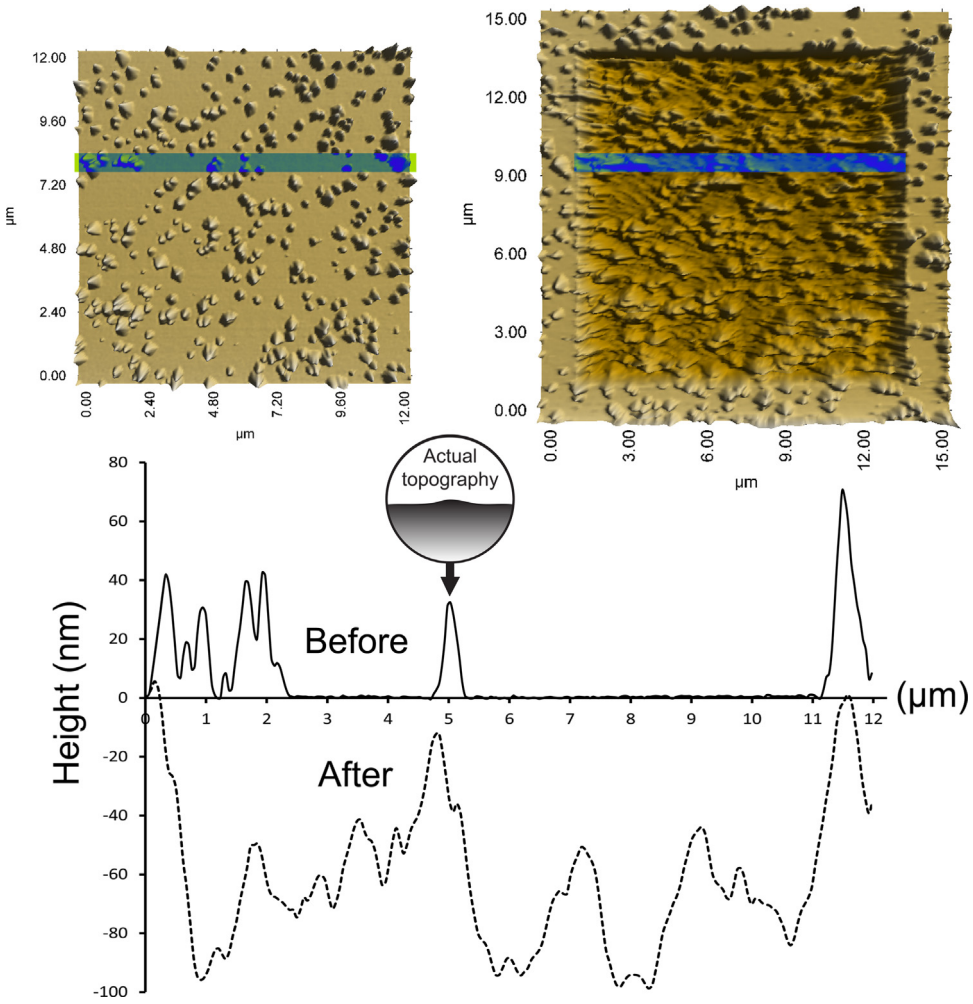

Fig. 1. SPM images and topography cross-section (marked with colored box) of sample B (200 °C, 100 nm) before and after scanning nanowear testing with 40 μN load. Note that the height and lateral axes are not in the same scale (nm vs μm) which emphasizes the height scale. The crystallite agglomerates protrude up to 70 nm from the amorphous/nanocrystalline matrix level and they were up to 37 ± 10%-points more wear-resistant than the matrix. (For interpretation of the references to color in this figure legend, the reader is referred to the web version of this article.)

Table 3
Film composition and impurity concentration from TOF-ERDA measurements. Films under 100 nm were not measured and the film composition was expected to be the same as with 100 nm.

Sample	Ti (at%)	O (at%)	H (at%)	C (at%)	Cl (at%)
A (110 °C, 100 nm)	32 ± 1	65 ± 2	1.0 ± 0.2	0.20 ± 0.05	1.9 ± 0.1
B (200 °C, 100 nm)	34 ± 1	66 ± 2	0.20 ± 0.05	< 0.1	0.34 ± 0.03
C (300 °C, 100 nm)	33 ± 2	67 ± 2	< 0.05	< 0.05	< 0.05

Table 4
Hardness and elastic modulus from nanoindentation measurements (in calculation, value of ν_{TiO2} = 0.28 was used).

Sample	Hardness (GPa)	Elastic modulus (GPa)	Residual stress (MPa)[a]
A (110 °C, 100 nm)	6.9 ± 0.1	152.2 ± 5.0	400 ± 130
B (200 °C, 100 nm)	8.5 ± 1.0	154.4 ± 8.3	810 ± 190
C (300 °C, 100 nm)	9.7 ± 1.0	165.2 ± 16.3	480 ± 190
D (300 °C, 50 nm)	11.2 ± 0.7	169.6 ± 10.1	580 ± 130
E (300 °C, 15 nm)	12.1 ± 1.1	169.3 ± 10.1	580 ± 340

[a] Residual stresses were measured from similar films deposited using the same process parameters.

3.4. Nanotribological and interfacial properties

SEM images of all of the samples after the tribological testing can be seen in Fig. 2 for the temperature series and in Fig. 3 for the thickness series.

The results of the wear depth analysis can be found in Fig. 4. The average wear depth with different wear loads is shown as a function of hardness. Each hardness value represents one sample type and the corresponding growth temperature and thickness can be seen above the data series. The error bars represent the standard deviation of the wear depth measurements. The biggest transition in the graph can be seen between the deposition temperatures of 200 °C and 300 °C where the wear depth decreases significantly.

SEM images of film fracture analysis can be seen in Fig. 5.

4. Discussion

4.1. Film thickness, density and crystallinity

At 110 °C the film was amorphous and at 300 °C the film was fully crystalline (anatase phase). The most interesting sample in terms of crystallinity was the 200 °C sample which had a composite-like mixture of protruding anatase crystallite agglomerates in an amorphous/nanocrystalline matrix also increasing the

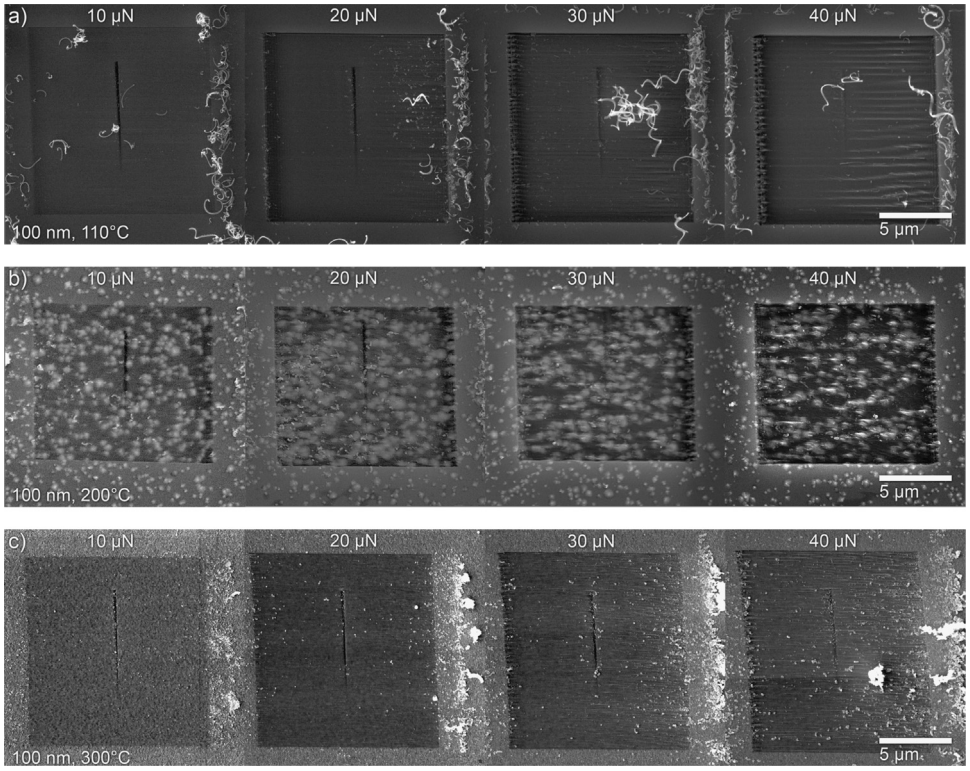

Fig. 2. SEM images of the temperature series after nanoscratch and scanning nanowear testing with 10, 20, 30 and 40 μN loads, respectively. (a) 110 °C, 100 nm (b) 200 °C, 100 nm (c) 300 °C, 100 nm. Some wear debris was left in the wear-test area even after the imaging scan.

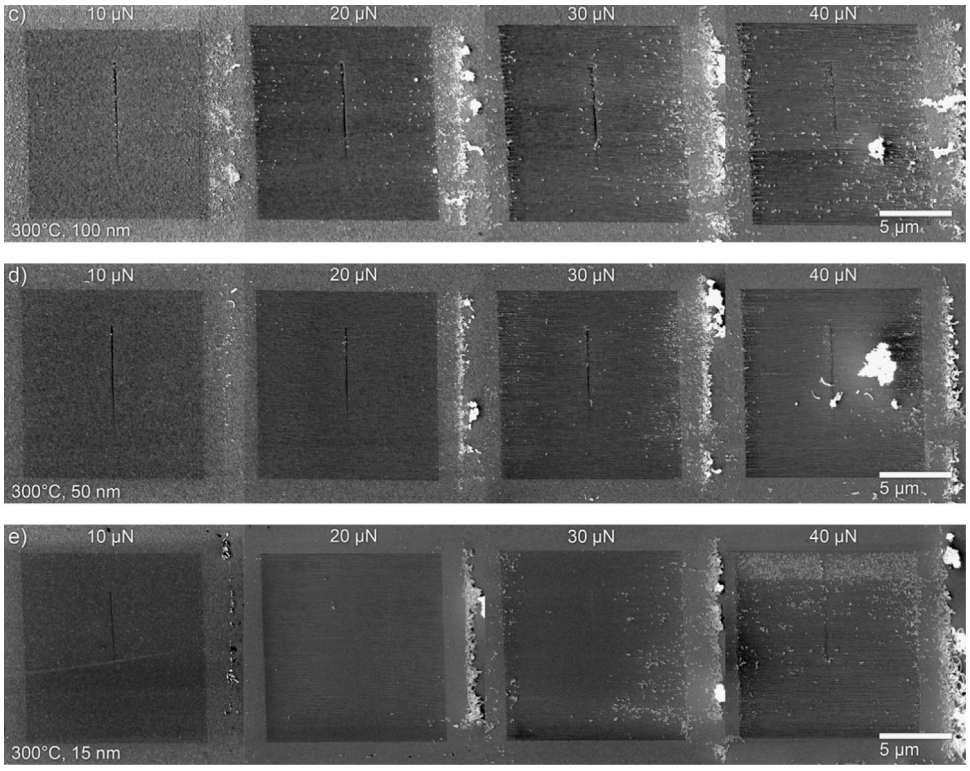

Fig. 3. SEM images of the thickness series deposited at 300 °C after nanoscratching and scanning nanowear testing with 10, 20, 30 and 40 μN loads, respectively. (c) 100 nm, (d) 50 nm and (e) 15 nm film. Some wear debris was left in the wear-test area even after the imaging scan.

residual stress of the coating significantly. The agglomerates of smaller fused crystallites are columnar reaching all the way to the substrate and their size increases slightly towards the substrate based on the SPM measurements after wear testing: the diameter of the agglomerates is increasingly larger when going deeper inside the material with increasing wear load. Possible tip artifacts can be formed to the SPM images if the side walls of the 90° tip with radius of 40 nm collides with large holes or peaks with a

sidewall angle of above 90° on the surface. To be noted in Fig. 1, the axis scales are not in the same scale (nm vs μm) which will over-exaggerate the true topography of the surface especially in the height scale. SEM images show the real scale topography and for clarification, an example of the true topography can also be seen in Fig. 1 from which can be clearly seen that the sidewalls of the agglomerates are well below the angle of 90° not producing tip artifacts.

The amorphous to crystalline transition is in agreement with the literature: The structure of the TiO_2 film depends on the deposition temperature, film thickness, substrate material and crystallization kinetics [32–35]. Puurunen et al. studied the controllability of crystallinity and roughness of TiO_2 films deposited at 110–300 °C on different substrates. They propose the following scheme for the growth mechanism of crystalline TiO_2: TiO_2 growth begins as amorphous film and crystallite nuclei form after a certain thickness has been reached. Further deposition adopts the crystalline structure of the nuclei, and crystalline grains grow. After a while, the remaining amorphous phase next to the crystalline grains starts to crystallize eventually extending the crystallites throughout the film [32]. Our observations support this proposition when comparing films grown at 200 °C from 100 nm to 300 nm [24] as can be seen in Fig. 6.

Kim et al. observed a similar amorphous-mixed structure-crystalline transition using cross-sectional high-resolution transmission electron microscopy (HRTEM), glancing angle X-ray diffraction (GAXRD) and AFM. They studied 5–60 nm thick films deposited at 200–330 °C from Ti[OCH(CH3)2]4 (TTIP) - H_2O precursors on Ru and Si substrates [33]. Jõgi et al. report amorphous/crystalline phase transformation with TiO_2 films deposited at a temperature over 175 °C [34]. Reiners et al. show pyramid shaped anatase crystallites present in TiO_2 deposited on Al_2O_3, Ti and Si, but not on SiO_2 and RCA-cleaned Si substrates in the amorphous TiO_2 matrix similar to our films. They also note that the hydroxylic group density is enhanced for the anatase facets which promotes further crystal growth [35].

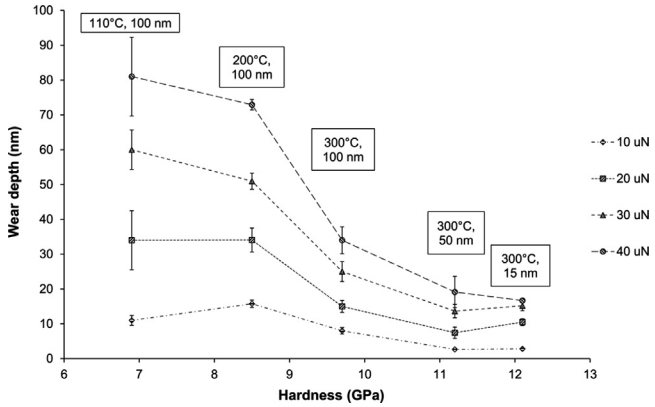

Fig. 4. Average wear depth measured from the test area of 12 × 12 μm with different wear loads as a function of hardness. Each hardness value represents one sample type. The corresponding growth temperature and thickness can be seen above the data series. The error bars represent the standard deviation of the wear depth measurements.

4.2. Hardness, elastic modulus and residual stress

The hardness of the samples increased with the deposition temperature probably due to phase transformation from amorphous film (110 °C) to a mixture of amorphous/nanocrystalline anatase film (200 °C) to fully crystalline anatase film (300 °C). The thinner films were also slightly harder than thicker films. The effects of the substrate are increasingly difficult to be excluded when testing thinner films even though the "use the maximum indentation depth of 10% of the film thickness" rule of thumb was used in the measurements. The film density was higher with 200 °C and 300 °C films compared to the 110 °C film which had higher H and Cl impurity concentration. The residual stresses were the highest for the 200 °C film which was most probably the result of the amorphous/nanocrystalline structure visible in Fig. 2 (b) and Fig. 6(a). The internal stress was lower with the 300 °C sample, which was probably due to relaxation after the phase transformation from amorphous to fully crystalline anatase phase

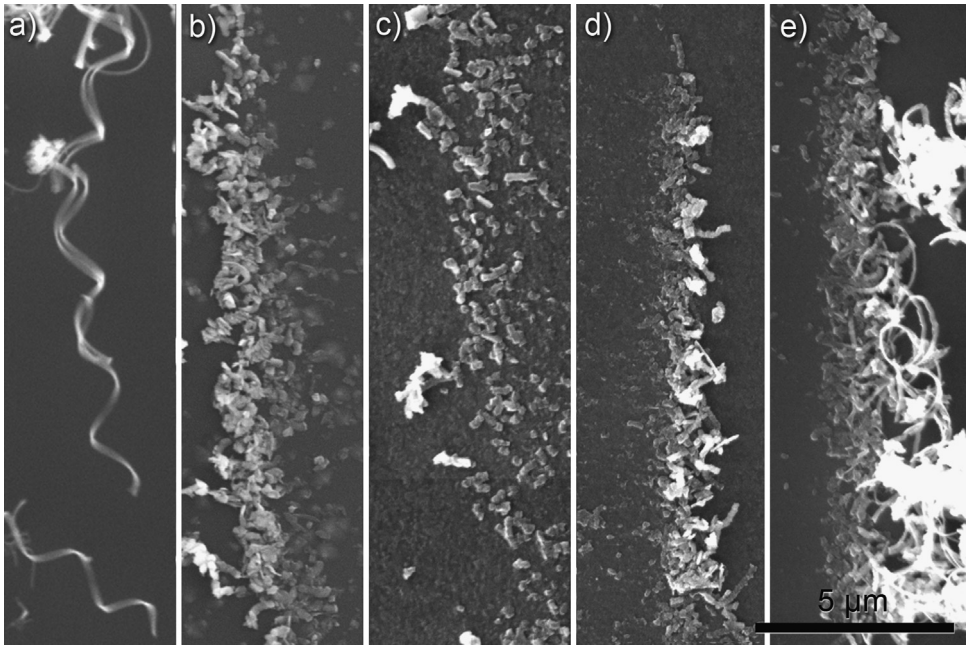

Fig. 5. Fractured film strips as a result of two-body abrasive wear. The strips are moved away from the wear test area after the imaging scan. (a) 110 °C, 100 nm (b) 200 °C, 100 nm (c) 300 °C, 100 nm (d) 300 °C, 50 nm and (e) 300 °C, 15 nm.

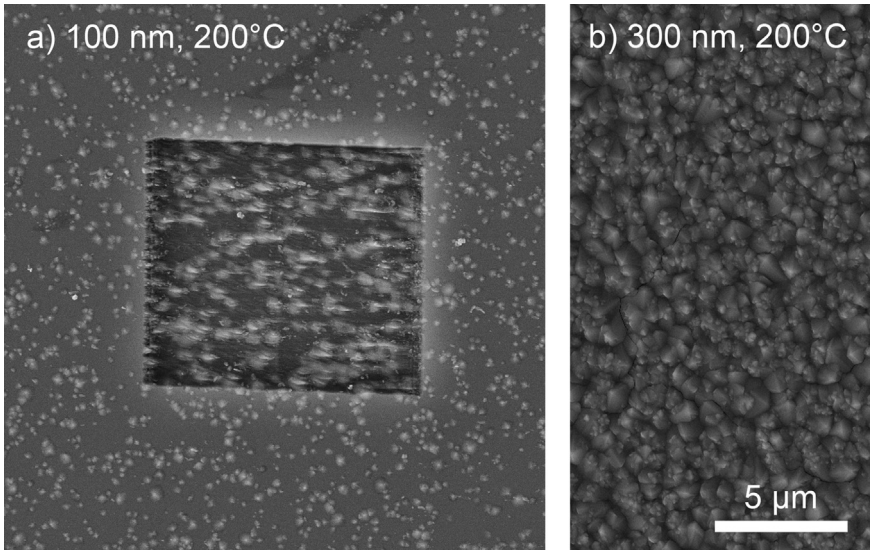

Fig. 6. SEM images of (a) 100 nm thick TiO_2 deposited at 200 °C after scanning nanowear testing shows a mixture of anatase crystallites in an amorphous/nanocrystalline matrix. (b) 300 nm thick TiO_2 deposited at 200 °C shows fully crystalline structure. (300 nm sample was characterized earlier [24]).

was complete. The values of elastic modulus were in good accordance with the literature [36,37].

4.3. Nanotribological and interfacial properties

All of the tested films had excellent interfacial mechanical properties as the film adhesion to the substrate was higher than the cohesion or fracture toughness of the films. No delamination was observed with the films outside of the wear test area and no significant delamination was observed near the scratches, which is a sign of excellent thin film adhesion. For reference, when the films were tested using larger scale microscratch testing, the silicon substrate always broke before the film was delaminated [38]. One of the main points of this study was to focus the loading more to the film and to the interface instead of the substrate. Utilizing the significantly sharper tip in the nanoscratching and scanning nanowear (40 nm tip radius compared to the 20 μm HRC tip used in the microscratch testing) the loading to the substrate was not as strong and thus the goal to focus the loading more to the film and to the interface succeeded. This characterization method is thus useful in studying the nanotribological, nanomechanical and interfacial properties of increasingly thinner films. Abrasive wear was observed as the sharp-edged 90° cube corner tip performed the scanning wear testing and the resulting strips of the fractured film are visible in Fig. 5. After the wear testing the wear track was imaged using the SPM, which moved most of the abraded film strips away from the wear track. The amorphous 100 °C, 100 nm film showed more cohesive ductile behavior and the fractured strips were continuous and long as can be seen in Fig. 5(a). The 300 °C, 15 nm film also showed cohesive ductile behavior with continuous and long strips. The thinner film has not yet fully crystallized due to the small thickness and shorter process time which kinetically seems too short for full phase transformation from amorphous to crystalline structure. When increasing the film thickness to 50 and 100 nm the degree of crystallization increased and the fracture behavior transitioned towards brittle fracture as the strips were shorter and more non-continuous crystalline grains. With the 50 and 100 nm thick films the process time is longer which facilitates phase transformation from amorphous to crystalline. The residual stress also decreased with the thicker films.

Thin film wear increased with increasing the scanning nanowear load as is expected. Clear transition in wear behavior was observed especially with the temperature series. Between 110 °C and 200 °C crystallization begins and as the crystallization is complete at 300 °C the enhanced wear-resistance is more dramatic. For the thickness series the wear behavior was more linear. In general, films deposited at lower temperatures had higher wear compared to the films deposited at higher temperatures. This is due to the lower hardness of the films as is shown in Fig. 4. Also film crystallinity seems to have an effect on the mechanical durability of the films. At 200 °C the film includes amorphous/nanocrystalline and anatase phases and the agglomerated anatase crystallites seem to be mechanically more durable than the amorphous/nanocrystalline phase resulting in selective wear. The agglomerated crystallites of the 200 °C film were up to $37 \pm 10\%$-points more wear-resistant than the amorphous/nanocrystalline matrix (measured from 5 individual crystallite agglomerates for each wear load).

In terms of potential applications for this controlled nanowear besides nanotribological and interfacial testing, it could be used as nanomachining to mechanically manufacture tailored structures in the nanoscale, although it might not be economic or efficient in the large scale production.

4.4. Finite element modeling

Kurapati used finite element analysis to simulate deep indentation of strain-hardening elastoplastic materials by a rigid spherical indenter with two types of systems: soft film–hard substrate and hard film–soft substrate systems. For soft film–hard substrate systems the maximum von Mises stress was under the indenter in the thin film. For hard film–soft substrate systems the maximum von Mises stress was at the thin film side of the interface against the substrate, suggesting a higher risk for delamination of the coating [39]. In our case the film hardnesses were between 6.9 ± 0.1 GPa and 12.1 ± 1.1 GPa. The hardness of undoped (100) silicon is 12.5 ± 0.5 GPa [40] so our case can be approximated using the soft film–hard substrate system model, where the maximum von Mises stress was between the indenter and the film.

5. Conclusions

A novel combination of nanoscratching and scanning nanowear was presented to study the nanotribological, nanomechanical and interfacial properties of different ALD TiO_2 thin films and to compare different film properties to offer guidelines in material selection for actual applications. The main motivation was in the development of the characterization methods to focus the loading mainly to the film and the interface instead of the substrate as is the case in larger scale microscratching.

The pre-scratch was created to facilitate thin film debonding, but the film cohesion was lower than film adhesion to the substrate resulting in varying amounts of two-body abrasive wear with all of the tested coatings. The relationship with deposition temperature and the effect of partial and full crystallization was compared to the wear resistance and fracture properties of the coatings. Higher deposition temperatures resulted in harder films as well as transition from amorphous to crystalline structures. Harder coatings were more wear-resistant as expected. Crystalline films (anatase phase) and the crystalline phase of a partially crystallized film were also harder and more wear resistant than amorphous/nanocrystalline films. The fracture behavior was more cohesive and ductile for the low temperature and the thinnest sample which will enable easier control in nanomachining. For all of the other films the fracture behavior was brittle and the fractured film strips were shorter crystalline grains which might cause unwanted fracture patterns in nanomachining. All of the films had excellent interfacial mechanical durability and adhesion to the substrate signifying high tolerance for nanomachining and for practical applications.

These findings may prove useful in the development of nanotribological, nanomechanical and interfacial characterization methods, and in developing thin film materials with enhanced properties tailored to their function. This will also help in the development and tuning of ALD processes as well as with controlled nanomachining to manufacture three dimensional nanostructures.

Acknowledgments

This work has been partially conducted within the MECHALD Project (389/31/2011) funded by Tekes (the Finnish Funding Agency for Technology and Innovation), partially by funding from Aalto University, School of Chemical Technology (125/FS.D/2014, 19.9.2014). The work is linked to the Finnish Centre of Excellence in Atomic Layer Deposition by the Academy of Finland. The work has been conducted in the Research Group for Physical Characteristics of Surfaces and Interfaces (PCS) at Aalto University. All of the ALD depositions were done at VTT in Micronova Nanofabrication Center. Thanks to doctoral candidate Oskari Elomaa for scientific expertise and advice in the reviewing of the manuscript.

References

[1] F. Gao, S. Arpiainen, R.L. Puurunen, Microscopic silicon-based lateral high-aspect-ratio structures for thin film conformality analysis, J. Vac. Sci. Technol. A 33 (2015) 010601.
[2] V. Miikkulainen, M. Leskelä, M. Ritala, R.L. Puurunen, Crystallinity of inorganic films grown by atomic layer deposition: overview and general trends, J. Appl. Phys. 113 (2013) 021301.
[3] R.L. Puurunen, Surface chemistry of atomic layer deposition: A case study for the trimethylaluminum/water process, J. Appl. Phys. 97 (2005) 121301.
[4] R.L. Puurunen, A short history of atomic layer deposition: Tuomo Suntola atomic layer epitaxy, Chem. Vapor Depos. 20 (2014) 332.
[5] S.M. George, Atomic layer deposition: an overview, Chem. Rev. 110 (2010) 111.
[6] M. Ritala, J. Niinistö, Industrial applications of atomic layer deposition, ECS Trans. 25 (8) (2009) 641.
[7] C.-T. Wang, H.-L. Siao, Improving photovoltaic performance of titanium oxide thin films by integration of iron doping and dye sensitization, Surf. Coat. Technol. 244 (2014) 63.
[8] T.-T. Duong, Y.-J. Kim, J.-H. Eom, J.-S. Choi, A.-T. Le, S.-G. Yoon, Enhancement of solar cell efficiency using perovskite dyes deposited via a two-step process, RSC Adv. 5 (2015) 33515.
[9] E. Marin, A. Lanzutti, M. Lekka, L. Guzman, W. Ensinger, L. Fedrizzi, Chemical and mechanical characterization of TiO_2/A_2O_3 atomic layer depositions on AISI 316 L stainless steel, Surf. Coat. Technol. 211 (2012) 84.
[10] H. Yaghoubi, N. Taghavinia, E.K. Alamdari, Self cleaning TiO2 coating on polycarbonate: Surface treatment, photocatalytic and nanomechanical properties, Surf. Coat. Technol. 204 (2010) 1562.
[11] C. Xu, A. Cui, Y. Xu, X. Fu, Graphene oxide–TiO_2 composite filtration membranes and their potential application for water purification, Carbon 62 (2013) 465.
[12] W.S. Law, S.W. Lam, W.Y. Gan, J. Scott, R. Amal, Effect of film thickness and agglomerate size on the superwetting and fog-free characteristics of TiO_2 films, Thin Solid Films 517 (2009) 5425.
[13] Y. Xiong, M. Lai, J. Li, H. Yong, H. Qian, C. Xu, K. Zhong, S. Xiao, Facile synthesis of ultra-smooth and transparent TiO_2 thin films with superhydrophilicity, Surf. Coat. Technol. 265 (2015) 78.
[14] C.C. Trapalis, P. Keivanidis, G. Kordas, M. Zaharescu, M. Crisan, A. Szatvanyi, M. Gartner, $TiO_2(Fe^{3+})$ nanostructured thin films with antibacterial properties, Thin Solid Films 433 (2003) 186.
[15] G. Koşarsoy, E.H. Şen, N. Aksöz, S. İde, H. Aksoy, TiO_2 nanocomposites: preparation, characterization, mechanical and biological properties, Appl. Surf. Sci. 318 (2014) 269.
[16] X. Wang, J. Zhang, W. Sun, W. Yang, J. Cao, Q. Li, Y. Peng, J.K. Shang, Anti-algal activity of palladium oxide-modified nitrogen-doped titanium oxide photocatalyst on *Anabaena* sp. PCC 7120 and its photocatalytic degradation on Microcystin LR under visible light illumination, Chem. Eng. J. 264 (2015) 437.
[17] K.L. Mittal, Adhesion measurement of thin films, Electrocompon. Sci. Technol. 3 (1976) 21.
[18] K.L. Mittal, T. Ahsan, Adhesion in Microelectronics, first ed., John Wiley & Sons, Inc., Hoboken, New Jersey, 2014, and Scrivener Publishing LLC, Salem, Massachusetts.
[19] A.A. Volinsky, N.R. Moody, W.W. Gerberich, Interfacial toughness measurements for thin films on substrates, Acta Mater. 50 (2002) 441.
[20] R. Lacombe, Adhesion measurement methods, theory and practice, first ed., CRC Press, New York, 2006.
[21] V. Liimatainen, J. Venälainen, M. Koverola, Q. Zhou, J. Lyytinen, J. Koskinen, V. Rontu, M. Berdova, S. Franssila, Characterization of nano-coated micro- and nanostructures by pushing, in: Proceedings of International Conference on 3M-NANO,7057329, 2014, pp. 23–27.
[22] M. Berdova, J. Lyytinen, K. Grigoras, A. Baby, L. Kilpi, H. Ronkainen, S. Franssila, J. Koskinen, Characterization of thin film adhesion by MEMS shaft-loading blister testing, J. Vac. Sci. Technol. A 31 (2013) 031102.
[23] J. Lyytinen, M. Berdova, S. Franssila, J. Koskinen, Adhesion testing of atomic layer deposited TiO_2 on glass substrate by the use of embedded SiO_2 microspheres, J. Vac. Sci. Technol. A 32 (2014) 01A102.
[24] J. Lyytinen, M. Berdova, P. Hirvonen, X.W. Liu, S. Franssila, Q. Zhou, J. Koskinen, Interfacial mechanical testing of atomic layer deposited TiO_2 and Al_2O_3 on a silicon substrate by the use of embedded SiO_2 microspheres, RSC Adv. 4 (2014) 37320.
[25] O.M.E. Ylivaara, X.W. Liu, L. Kilpi, J. Lyytinen, D. Schneider, M. Laitinen, J. Julin, S. Ali, S. Sintonen, M. Berdova, E. Haimi, T. Sajavaara, H. Ronkainen, H. Lipsanen, J. Koskinen, R.L. Puurunen, Aluminum oxide from trimethylaluminum and water by atomic layer deposition: the temperature dependence of residual stress, elastic modulus, hardness and adhesion, Thin Solid Films 552 (2014) 124.
[26] S. Sintonen, S. Ali, O.M.E. Ylivaara, R.L. Puurunen, H. Lipsanen, X-ray reflectivity characterization of atomic layer deposition Al_2O_3/TiO_2 nanolaminates with ultrathin bilayers, J. Vac. Sci. Technol. A 32 (2014) 01A111.
[27] Stoney, 1909 G.G. Stoney, The tension of metallic films deposited by electrolysis, in: Proceedings of the Royal Society of London, Series A 82, 1909, pp. 172.
[28] W.A. Brantley, Calculated elastic constants for stress problems associated with semiconductor devices, J. Appl. Phys. 44 (1973) 534.
[29] M. Laitinen, M. Rossi, J. Julin, T. Sajavaara, Time-of-flight – energy spectrometer for elemental depth profiling – Jyväskylä design, Nucl. Instrum. Methods B 337 (2014) 55.
[30] W.C. Oliver, G.M. Pharr, An improved technique for determining hardness and elastic modulus using load and displacement sensing indentation experiments, J. Mater. Res. (1992) 1564.
[31] A.C. Fischer-Cripps, Introduction to Contact Mechanics, in: Nanoindentation, 19, Springer, New York, 2011.
[32] R.L. Puurunen, T. Sajavaara, E. Santala, V. Miikkulainen, T. Saukkonen, M. Laitinen, M. Leskelä, Controlling the crystallinity and roughness of atomic layer deposited titanium dioxide films, J. Nanosci. Nanotechnol. 11 (2011) 8101.
[33] W.D. Kim, G.W. Hwang, O.S. Kwon, S.K. Kim, M. Cho, D.S. Jeong, S.W. Lee, M. H. Seo, C.S. Hwang, Y.-S. Min, Y.J. Cho, Growth characteristics of atomic layer deposited TiO_2 thin films on Ru and Si electrodes for memory capacitor applications, J. Electrochem. Soc. 152 (2005) C552.
[34] I. Jõgi, M. Pärs, J. Aarik, A. Aidla, M. Laan, J. Sundqvist, L. Oberbeck, J. Heitmann, K. Kukli, Conformity and structure of titanium oxide films grown by atomic layer deposition on silicon substrates, Thin Solid Films 516 (2008) 4855.

[35] M. Reiners, K. Xu, N. Aslam, A. Devi, R. Waser, S. Hoffmann-Eifert, Growth and crystallization of TiO_2 thin films by atomic layer deposition using a novel amido guanidinate titanium source and tetrakis-dimethylamido-titanium, Chem. Mater. 25 (2013) 2934.
[36] A. Bendavid, P.J. Martin, H. Takikawa, Deposition and modification of titanium dioxide thin films by filtered arc deposition, Thin Solid Films 360 (2000) 241.
[37] L. Borgese, M. Gelfi, E. Bontempi, P. Goudeau, G. Geandier, D. Thiaudière, L. E. Depero, Young modulus and Poisson ratio measurements of TiO_2 thin films deposited with atomic layer deposition, Surf. Coat. Technol. 206 (2012) 2459.
[38] O.M.E. Ylivaara, X. Liu, L. Kilpi, D. Schneider, M. Laitinen, J. Julin, S. Ali, S. Sintonen, E. Haimi, T. Sajavaara, H. Lipsanen, H. Ronkainen, S.-P. Hannula, R.L. Puurunen, Temperature dependence of the mechanical properties of ALD TiO_2 from $TiCl_4$ and H_2O on silicon, in: Proceedings of the 12th International Baltic Conference on Atomic Layer Deposition, Helsinki, May 12–13, 2014, oral presentations.
[39] Siva N.V.R. Kurapati, Elastic–Plastic Indentation Deformation in Homogeneous and Layered Materials: Finite Element Analysis (Master's theses) University of Kentucky, Paper 576, 2008, ⟨http://uknowledge.uky.edu/gradschool_theses/576⟩.
[40] Bharat Bhushan, Xiaodong Li, Micromechanical and tribological characterization of doped single-crystal silicon and polysilicon films for microelectromechanical systems devices, J. Mater. Res. 12 (1997) 59.